Thermoelasticity-based modal damage identification

Lorenzo Capponi[a], Janko Slavič[b,1], Gianluca Rossi[c], Miha Boltežar[b]

[a] *University of Padova, CISAS G. Colombo, via Venezia 15, 35131 Padova, Italy*
[b] *University of Ljubljana, Faculty of Mechanical Engineering, Aškerceva 6, 1000 Ljubljana, Slovenia*
[c] *University of Perugia, Department of Engineering, via G. Duranti 93, 06125 Perugia, Italy*

Cite as:
Lorenzo Capponi, Janko Slavič, Gianluca Rossi, Miha Boltežar, Thermoelasticity-based modal damage identification, International Journal of Fatigue, 2020, ISSN 0142-1123, doi.org/10.1016/j.ijfatigue.2020.105661.

Abstract

The response of linear dynamic structures can be decomposed into modal components, where each natural frequency is also represented by a corresponding mode shape and damping ratio. While vibration-fatigue-damage identification was recently expanded using modal decomposition, this research proposes a modal-decomposition-based thermoelastic damage identification method. With the proposed method, a thermal camera can be used to identify the damage intensity of a particular mode shape. The proposed method is presented using a randomly excited structure exposed to multiaxial loads. With this, the intensity of a particular fatigue source is clearly related to the underlying structural dynamics.

Keywords: thermoelasticity, fatigue damage, modal decomposition, frequency-domain

1. Introduction

When a flexible structure is excited at or close to one of its natural frequencies, significantly increased fatigue damage occurs [1, 2]. Frequency-domain fatigue-life estimation methods are mostly preferred to time-domain approaches for process description and computational efficiency reasons [3]. The damage assessment is closely related to the structural dynamics, which is generally observed in the frequency-domain [4, 5]. Furthermore, in reality, structures are generally subjected to random loads, which are usually described in the frequency domain by a power spectral density [6, 7, 5]. Moreover, only a subgroup of modes generally participates in the structural response for the frequency range of interest, in this case, modal reduction can be carried out and the efficiency of

[1] Corresponding author. Tel.: +386 14771 226. Email address: janko.slavic@fs.uni-lj.si

the frequency-based methods is increased [8]. In fact, in the past two decades, several spectral damage-estimation methods have been developed [3], *e.g.*, Dirlik [9], Gao-Moan [10], Petrucci-Zuccarello [6], Tovo-Benasciutti [4], Wirsching-Light [11] and Zhao-Baker [12]; Mršnik *et al.* [3] found that the Tovo-Benasciutti method with its better theoretical explanation is also more accurate than the Dirlik method. Moreover, in past few years, numerous frequency-domain-based multiaxial damage-estimation criteria have been developed [13, 14, 15]. Experimental and numerical research has been conducted by Zhou and Tao [16] and Benasciutti *et al.* [17]. Mršnik *et al.* [18] and Morettini *et al.* [19] compared numerical methods and created a multiaxial fatigue parameters database, respectively. Mršnik *et al.* [20] also proposed the modal decomposition approach in order to obtain the damage contribution of each participating mode.

In recent years the use of non-contact image-based measurement techniques in structural dynamics applications has grown. Displacements and deformations can be measured with cameras operating in the visible spectrum by applying both digital-image-correlation and computer-vision methods [21, 22]. Furthermore, image-based modal analysis [23, 24, 25] and non-destructive testing algorithms have also been developed [26]. On the other hand, by operating in the infrared spectrum, thermoelastic stress analysis is one of the most used methods in order to perform image-based stress measurements [27, 28]. This technique is based on the thermoelastic effect, which relates, for a dynamically loaded structure, surface-temperature fluctuations to stress- and strain-tensor changes. Thermoelasticity has the advantage of being non-contact, full-field and having a high sensitivity comparable to standard local stress measurement methods (i.e., strain gauges). Thermoelastic stress analysis has been widely used for non-destructive testing. Defect identification was researched by Guo and Mao [29], while Allevi *et al.* [30] used it for characterising plastic and metallic materials. Thermoelasticity has also been used to determine the stress-intensity factor and crack propagation, as well as fatigue-limit parameters [31]. In particular, Qiu *et al.* in [32] proposed laser-spot thermography for a quantitative estimation of surface cracks and Li *et al.* [33] researched the damage characteristics of carbon-fiber laminates. An increasing temperature in the time domain during an excitation load has been considered by Fargione *et al.* [34] as a fatigue-damage indicator [35]. On the other hand, frequency-domain methods have been proposed by Stankovičová *et al.* [36] and Braccesi *et al.* [37] in order to perform a modal analysis via a lock-in approach and to obtain a damage estimation with an IR camera, respectively. Previous research showed that a thermoelasticity-based spatial damage intensity evaluation is possible [36]; however, the relation of the identified damage was not decomposed to particular mode shapes of the dynamic structure.

In this research thermoelasticity-based damage identification is investigated with respect to the underlying structural dynamics, *i.e.*, to particular mode shapes. This manuscript is organized as follows. In Sec. 2 the theoretical background is given on thermoelasticity, thermal image processing, vibration fatigue and thermoelasticity-based damage intensity. Sec. 3 introduces the thermoelasticity-based modal damage identification. In Sec. 4 the measurement

setup and the results of the experimental research are presented and discussed. Finally, Sec. 5 draws the conclusions.

2. Theoretical background

2.1. Thermoelasticity

Thermoelasticity, also known as Thermoelastic Stress Analysis (TSA), is a full-field non-contact measurement technique based on the thermoelastic effect [27, 28]. According to this effect, if a structure is cyclically excited, its surface-temperature response variations are proportional to the change in the stress- and strain-tensor traces [38]. The theoretical foundation of thermoelasticity arises from both thermodynamics and continuum mechanics laws [39]. For a closed system undergoing a reversible process, from the first law of thermodynamics, considering an elastic solid and introducing the Gibbs free energy relations, the following relation is obtained [40]:

$$\frac{\mathrm{d}q}{T} = \rho\, C_\sigma \frac{\mathrm{d}T}{T} + \frac{\partial \epsilon_{ij}}{\partial T}\, \mathrm{d}\sigma_{ij}, \tag{1}$$

where q is the heat transfer from the surroundings to the system, ρ is the material density, C_σ is the specific heat at constant stress (*i.e.*, pressure), T is the temperature and ϵ_{ij} and σ_{ij} are the components of the strain and stress tensors, respectively [41]. Considering an adiabatic process, $\mathrm{d}q = 0$, and isotropic material, $\partial \epsilon_{ij}/\partial T = \alpha\, \delta_{ij}$, where α is the thermal expansion coefficient and δ_{ij} is the Kronecker delta, Eq. (1) is simplified to:

$$\rho\, C_\sigma \frac{\mathrm{d}T}{T} = -\alpha\, \delta_{ij}\, \mathrm{d}\sigma_{ij} = -\alpha\, \left(\mathrm{d}\sigma_x + \mathrm{d}\sigma_y + \mathrm{d}\sigma_z\right) \tag{2}$$

where σ_x, σ_y and σ_z are the principal stresses.
Integrating Eq. (2) between the equilibrium states, the following is obtained:

$$\rho\, C_\sigma \frac{\Delta T}{T_0} = -\alpha\, \left(\Delta\sigma_x + \Delta\sigma_y + \Delta\sigma_z\right) \tag{3}$$

where ΔT is the temperature variation at the surface of the body and T_0 is the ambient temperature. Under plane-stress isotropy (*i.e.*, $\Delta\sigma_z = 0$), the simplified formulation of thermoelasticity is [28]:

$$\Delta T = K_m \left(\Delta\sigma_x + \Delta\sigma_y\right), \tag{4}$$

where K_m is the thermoelastic coefficient [41]:

$$K_m = -\frac{\alpha\, T_0}{\rho\, C_\sigma}. \tag{5}$$

2.2. Thermal image processing

In general, the temperature variation caused by the thermoelastic effect is within the noise produced by the infrared detector. Thus, thermal acquisitions are necessarily post processed in order to obtain readable results [42]. A two-channel lock-in analysis is one of the most used techniques [43]; however, here a slightly generalized frequency-domain approach is used [44, 45]. In vibrating structures frequency-domain methods are reasonable and have been shown to enable displacement identification within the noise of the sensor; *e.g.* Javh *et al.* [23] successfully identified the amplitudes of oscillation at the level of $1/100{,}000^{\text{th}}$ of a pixel. The frequency-domain approach is typically based on the Discrete Fourier Transform (DFT) [46] or the Power Spectral Density (PSD); DFT is for the N-points time series X defined as:

$$X(\omega) = \sum_{n=0}^{N-1} X_n \, \exp\left(-\mathrm{i}\,\frac{n\,\omega}{N}\right), \tag{6}$$

while the PSD is typically estimated using Welch's method [47, 48, 49]:

$$S_{xx}(\omega) = \frac{1}{q}\sum_{u=1}^{q}\frac{1}{T_w}\left|X_{T_{wu}}(\omega)\right|^2. \tag{7}$$

In Eq. (7) the time-domain data X is considered for length T, segmented in q windows, each of length T_w. In this research a rectangular window was used.

2.3. Vibration fatigue using modal decomposition

Vibration fatigue is generally related to the high-cycle fatigue of flexible structures [1]. Flexible structures can be represented by N-degrees of freedom (DOFs) systems using [50]:

$$M\,\ddot{x}(t) + D\,\dot{x}(t) + K\,x(t) = f(t) \tag{8}$$

where M, D and K are the mass, damping and stiffness matrices, while f and x are the excitation force and the displacements of the DOFs, respectively. Assuming a harmonic excitation $f(t) = F\,\mathrm{e}^{\mathrm{i}\omega t}$ and a response $x(t) = X\,\mathrm{e}^{\mathrm{i}\omega t}$, Eq. (8) can be written as [50]:

$$(K + \omega\,D - \omega^2\,M)\,X(\omega) = F(\omega) \tag{9}$$

The displacement-response amplitude is given by Eq.(9) as:

$$X(\omega) = (K + \omega\,D - \omega^2\,M)^{-1}\,F(\omega) = H(\omega)\,F(\omega) \tag{10}$$

where $H(\omega)$ defines the receptance matrix [50]. Using eigenvalues notation, the receptance matrix can be written in diagonal form [50]:

$$H(\omega) = \Phi\,[\omega_r^2\,(1+\eta_r) - \omega^2]^{-1}\,\Phi^T \tag{11}$$

where Φ is the mass-normalized matrix, r is the eigenvalue/mode index, ω_r and η_r are the natural frequency and the damping-loss factor, respectively. The solution $X(\omega)$ is given in terms of displacements, while for a fatigue-damage assessment the stress response $X_s(\omega)$ is required [20, 51]:

$$X_s(\omega) = \Phi^s \left[\omega_r^2 \left(1 + \eta_r\right) - \omega^2\right]^{-1} \Phi^T F(\omega) = H_{sf}(\omega) F(\omega) \tag{12}$$

where Φ^s is the stress modal matrix, and $H_{sf}(\omega)$ is the frequency-response function (FRF) from force to stress. The FRF for a system with N-modes is defined as [20, 50]:

$$H_{sf}(\omega) = \sum_{r=1}^{N} H_{sf}^r(\omega) = \sum_{r=1}^{N} \frac{A_r^s}{\omega_r^2 - \omega^2 + \mathrm{i}\eta_r\omega_r^2} \tag{13}$$

where $H_{sf}^r(\omega)$ is the r-th modal stress FRF and A_r^s is the stress modal constant matrix [52, 53].
Continuous systems have theoretically an infinite number of DOFs N, but typically only a small subset m of those modes (*i.e.* number of DOF) is within the frequency range of interest. In this case, modal reduction methods can be applied and the contribution of other (usually high-frequency) modes is neglected [54]. The FRF is defined for the reduced system from Eq. (13) as [20]:

$$\tilde{H}_{sf}(\omega) = \sum_{r=1}^{m<N} H_{sf}^r(\omega) \tag{14}$$

If the reduced modes can be considered as well separated, then the modal stress PSD can be approximated to [20]:

$$\tilde{S}_{ss}(\omega) = \sum_{r=1}^{m<N} \tilde{S}_{ss}^r(\omega) = \sum_{r=1}^{m<N} H_{sf}^r(\omega) \cdot S_{ff}(\omega) \cdot H_{sf}^{r*T}(\omega) \tag{15}$$

where S_{ff} is the power spectral density of the excitation and $\tilde{S}_{ss}^r(\omega)$ is the stress PSD contribution of the r-th mode.
Fatigue-damage-evaluation time-domain approaches typically refer to Palmgren-Miner's rule [55]:

$$D = \sum_i \frac{n_i}{N_i} \tag{16}$$

where D is the total fatigue damage, and n_i and N_i are the number of cycles and the number of cycles to failure at a particular stress amplitude, respectively. They are defined by the Wöhler diagram of the material, described by Basquin's equation [56]:

$$\sigma = BN^{-\frac{1}{k}} \tag{17}$$

where B and k are the fatigue strength and the fatigue exponent related to the endurance curve. Of the numerous methods developed in recent years [3], that of Benasciutti and Tovo [4, 8] is one of the most promising [3]. The fatigue damage

using the Benasciutti and Tovo method is calculated as a linear combination of the upper and lower fatigue-intensity limits, as follows [4]:

$$\bar{D}_{TB} = \left[b + (1-b)\,\alpha_2^{k-1} \right] \bar{D}_{NB} \tag{18}$$

where b is the numerical determined factor, α_1 and α_2 are the spectral width parameters and $\bar{D}_{NB}$ is the narrow-band process damage intensity, defined, respectively, by:

$$b = \frac{(\alpha_1 - \alpha_2)\,\left(1.112\,\left(1 + \alpha_1\,\alpha_2 - (\alpha_1 + \alpha_2)\right)\right)^{2.11\,\alpha_2} + (\alpha_1 - \alpha_2)}{(\alpha_2 - 1)^2} \tag{19}$$

$$\alpha_1 = \frac{m_1}{\sqrt{m_0\,m_2}} \qquad \alpha_2 = \frac{m_2}{\sqrt{m_0\,m_4}} \tag{20}$$

$$\bar{D}_{NB} = \nu_p\,C^{-1}\,\alpha_2\,\left(\sqrt{2\,m_0}\right)^k\,\Gamma\left(1 + \frac{k}{2}\right) \tag{21}$$

where ν_p is the peak intensity for broad-band processes, C is the material fatigue parameter and Γ is the Euler gamma function, while m_0, m_1, m_2 and m_4 are the 0-th, 1-st, 2-nd and 4-th spectral moments, respectively [57]:

$$\nu_p = \frac{1}{2\,\pi}\sqrt{\frac{m_4}{m_2}} \tag{22}$$

$$C = B^k \tag{23}$$

$$\Gamma(z) = \int_0^\infty t^{z-1}\,\mathrm{e}^{-t}\,\mathrm{d}t \tag{24}$$

$$m_i = \int_{-\infty}^{\infty} \omega^i\,\tilde{S}_{ss}(\omega)\,\mathrm{d}\omega \tag{25}$$

2.4. Thermoelasticity-based damage identification

For an elastic solid, under adiabatic conditions, the relationship between the changes in the surface temperature ΔT and in the stress-tensor trace $\Delta(tr(\sigma))$ is linear, Eq. (3) and Eq. (4). The proportionality between ΔT and $\Delta(tr(\sigma))$ is given by the thermoelastic coefficient K_m (5), see [58] for experimental details. The stress–strain relationship given by the linear elasticity [59] is defined as:

$$\Delta\sigma_x + \Delta\sigma_y = \frac{E}{1-\nu}\,\left(\Delta\epsilon_x + \Delta\epsilon_y\right) \tag{26}$$

where ν and E are the Poisson's ratio and the Young's modulus of the material, respectively. The approach used in this research relates the measured strain amplitude $\Delta\epsilon_x + \Delta\epsilon_y$ to the thermoelastic signal amplitude ΔT_{avg}, averaged over the region where the strain gauge is bonded. As will be discussed in Sec. 4,

a uniaxial strain load at the surface was used for the calibration of K_m. Under uniaxial conditions, Eq. (4) and Eq. (26) result in:

$$K_m = \frac{\Delta T_{avg}\,(1-\nu)}{E\,\Delta\epsilon} \tag{27}$$

Once the thermoelastic coefficient K_m is identified, the principal stress $\Delta\sigma(t)$ (assuming the other two principal stresses are negligible) at the surface can be identified from the temperature variation $\Delta T(t)$:

$$\Delta\sigma_{i,j}(t) = \frac{\Delta T_{i,j}(t)}{K_m} \tag{28}$$

where i and j are the indexes that identify the location of the pixels in the infrared detector matrix (not to be confused with the ij indexes of the stress- and strain-tensor components σ_{ij} and ϵ_{ij} in Eq. (1) and Eq. (2)). Later, the modal strain at the surface will be researched, where the principal stress perpendicular to the surface is zero; similarly, the second principal stress is also zero when a particular strain mode-shape is considered (due to the orthogonality property) [50].
Once the stress–temperature relation in the time-domain is defined, the frequency approaches discussed in Sec. 2 can be used. Welch's method is applied along each pixel's stress time-history to estimate the power spectral density of the stress response of the vibrating structure. Thus, combining Eq. (7) and Eq. (28), the entire stress PSD response of the i,j-th pixel $S_{ss_{i,j}}(\omega)$ is given by:

$$S_{ss_{i,j}}(\omega) = \frac{1}{q}\sum_{u=1}^{q}\frac{1}{T_w}\left|\Delta\sigma_{T_{wu_{i,j}}}(\omega)\right|^2 \tag{29}$$

As discussed in Sec. 2, once the entire stress PSD response is obtained, the spectral moments can be computed using Eq. (25), and the fatigue-damage intensity is estimated with classic methods. In this research Tovo-Benasciutti's [60] is used. With Eq. (18), the damage intensity $\bar{D}_{TB_{i,j}}$ is obtained for each pixel:

$$\bar{D}_{TB_{i,j}} = \bar{D}_{TB}\left(S_{ss_{i,j}}(\omega),\, C,\, k\right) \tag{30}$$

This approach gives information about the total damage that occurred at the surface of the structure. It is important to note here that for the damage identification of a particular mode, separate experiments would be required: one experiment for each mode.

3. Thermoelasticity-based modal damage identification

This study proposes a method to decompose the total damage and obtain the damage contribution given by each particular mode from a single experiment.
As discussed in Sec. 2, the stress PSD response $\tilde{S}_{ss_{i,j}}(\omega)$ is represented as the sum of the stress PSD responses $\tilde{S}^r_{ss_{i,j}}(\omega)$ of a particular mode (15). The mode

shapes are orthogonal [50] and, if also well separated, the stress PSD response $\tilde{S}^r_{ss_{i,j}}(\omega)$ of each mode can be used to determine the damage intensity of a particular mode [20]. If a particular mode is researched, then the amplitudes of the response far from the natural frequency corresponding to this particular mode are negligible. Consequently, this modal response can be considered as a narrow-band process. The stress amplitude is obtained from the stress-amplitude spectrum $\Delta\sigma_{i,j}(\omega_r)$, which is based on the Fourier transform of the stress-time histories $\Delta\sigma_{i,j}(t)$. The load of this particular mode is harmonic, defined with its natural frequency ω_r.
For the mode r the narrow-band damage at the pixel i, j is defined using Palmgren-Miner's rule:

$$\bar{D}_{r_{i,j}} = \frac{n_r}{N_{\sigma_{i,j}}}, \tag{31}$$

where n_r is the number of cycles per second related to the natural frequency of the mode:

$$n_r = \frac{\omega_r}{2\,\pi}. \tag{32}$$

$N_{\sigma_{i,j}}$ is the number of cycles to failure at a particular stress amplitude $\sigma_{i,j}$, as defined by Eq. (17):

$$N_{\sigma_{i,j}} = \left(\frac{B}{\Delta\sigma_{i,j}(\omega_r)}\right)^k. \tag{33}$$

Combining Eq. (31), Eq. (32) and Eq. (33), the modal damage $D_{r_{i,j}}$ is defined as:

$$\bar{D}_{r_{i,j}} = n_r \left(\frac{\Delta\sigma_{i,j}(\omega_r)}{B}\right)^k, \tag{34}$$

where the stress-amplitude spectrum $\Delta\sigma_{i,j}(\omega_r)$ is defined as (28):

$$\Delta\sigma_{i,j}(\omega_r) = \mathscr{F}\Big\{\frac{\Delta T_{i,j}(t)}{K_m}\Big\} \tag{35}$$

and $\Delta T_{i,j}(t)$ is the measured temperature variation at the pixel location i, j and $\mathscr{F}$ is the Fourier transform operator.

4. Experimental research

4.1. Measurement setup

In this research an aluminium-alloy Y-shaped specimen, shown in Fig. 1, was used [61]. In particular, this sample geometry was chosen due to its structural dynamics properties. In fact, by using two weights (each of 1054 g) fixed to each of the branches, the structural dynamics (*i.e.*, the mode shapes, natural frequencies and damping) were adjusted to the research needs. A similar multiaxial setup to that employed in [18] was used. The surface of the specimen was milled and fine ground. Then, a thin flat black coating was added to the surface, in order to obtain a uniform and enhanced surface emissivity [62, 63].

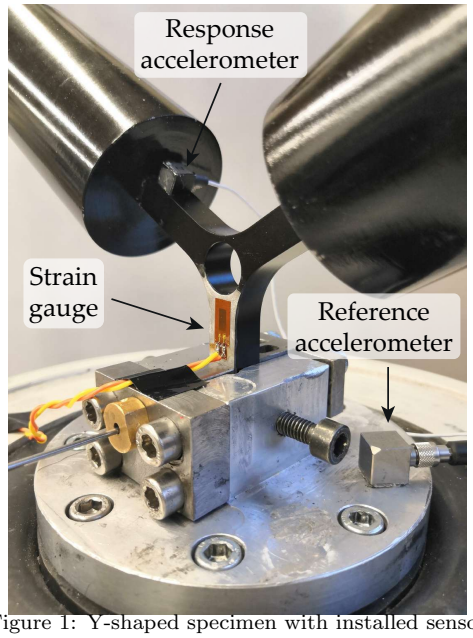

Figure 1: Y-shaped specimen with installed sensors

A multiaxial excitation test bench was set up using LDS V555 and LDS V406 electro-dynamical shakers, acting in the vertical and horizontal directions, respectively (Fig. 2). In particular, the V555 shaker was used as the primary shaker, which had its kinematics controlled by a closed-loop controller, while the second V406 shaker was used for dynamic excitation in the open loop. The V406 shaker was connected to the fixation between the Y-shaped sample and the V555 shaker using a stinger, as shown in Fig. 2, in order to have the optical access required for the thermal camera measurement and also enough space on the back side for the reference strain-gauge calibration procedure. The measurement setup also consists of a PCB T333B30 accelerometer and a PCB 208C01 force sensor used for monitoring the vertical and horizontal excitations, respectively. A triaxial Dytran 3133B1 accelerometer was installed on the specimen to measure its response and a HBM 1-LY13-6/350 strain gauge was attached and used for the calibration procedure, Fig. 1. The input signals were provided to the shakers through a NI-9263 DAC module and the measurements were made with the NI-9234 and NI-9237 ADC modules. During the test, the specimen's surface-temperature fluctuations were measured with a FLIR A6751sc cooled thermal camera, operating at a 400-Hz sampling rate and a spatial resolution of 128x160 pixels, focused on the critical fatigue area.

4.2. Thermoelastic coefficient identification

As discussed in Sec. 2, the strain gauge calibration procedure was performed in order to define the thermoelastic coefficient of the A-S8U3 aluminium alloy. The procedure involved a specimen made as the same material of the Y-shaped

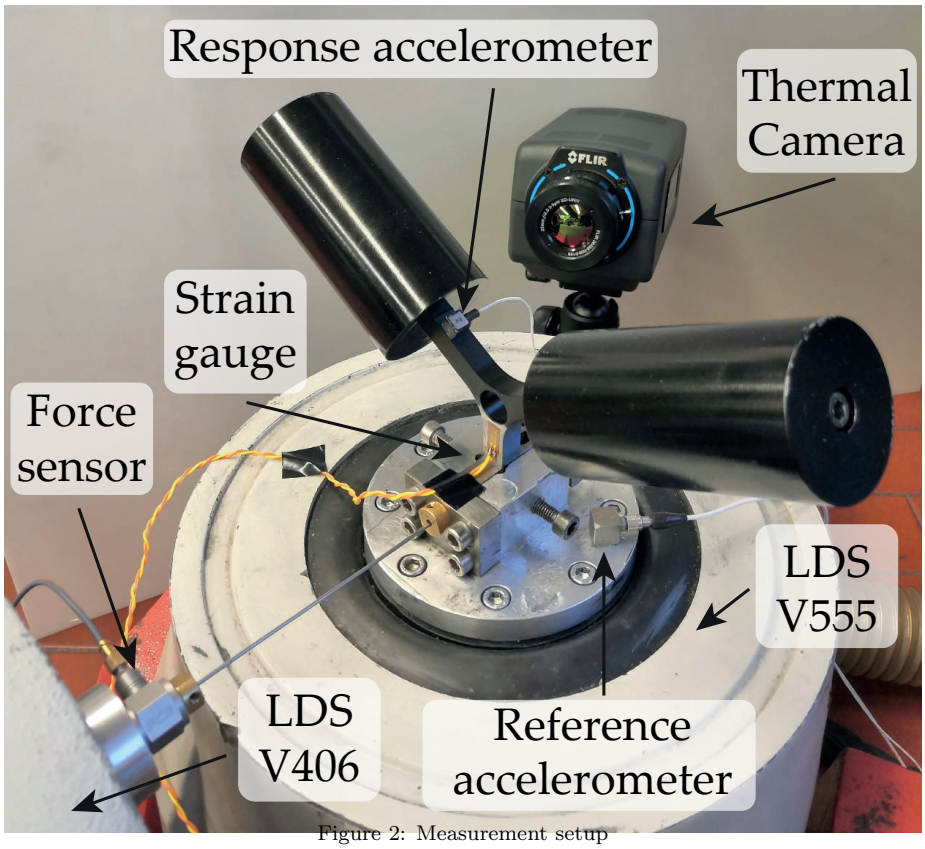

Figure 2: Measurement setup

sample, the same test environment and similar load conditions as the vibration-fatigue experiments. A strain gauge was attached to an area with a high signal-to-noise ratio (S/N) and a low strain gradient, see Fig. 1. The calibration specimen was harmonically loaded at 40 Hz and its surface's thermal response was measured [64]. The procedure was carried out on two different samples. A total of 32 measurements at different strain-amplitude levels (range of 1–10 $\mu\epsilon$) were obtained and then averaged to:

$$K_m = 1.2 \cdot 10^{-8} \pm 15\% \left[\frac{^\circ\mathrm{C}}{\mathrm{Pa}}\right] \tag{36}$$

4.3. Multiaxial excitation

The experimental modal analysis was initially made in order to obtain the entire FRF of the structure. The 1st and 2nd natural frequencies were determined as well separated at $f_1 \approx 33$ Hz and $f_2 \approx 55$ Hz, and the corresponding orthogonal mode shapes were considered. For the excitation, two flat-shaped PSD functions were defined: for the horizontal excitation the frequency band was from 23 Hz to 43 Hz and for the vertical excitation, the frequency band was from

45 Hz to 65 Hz. A total of 16 vibration tests at different RMS levels in the horizontal and vertical directions were made, see Tab. 1. In detail: initially, the horizontal excitation was at 4 [N^2/Hz] and the vertical was increased from 0.2 [$(m/s^2)^2$/Hz] to 0.8 [$(m/s^2)^2$/Hz] as given in the Tab. 1. Then the horizontal level was increased to level 8 [N^2/Hz] and again the vertical excitation level was increased as before. Similarly for horizontal levels of 12 [N^2/Hz] and 16 [N^2/Hz], resulting in a total of 16 experiments.

Table 1: Experimental excitation levels

	PSD level			
Vertical excitation [$(m/s^2)^2$/Hz]	0.2	0.4	0.6	0.8
Horizontal excitation [N^2/Hz]	4	8	12	16

During the several preliminary experiments performed in order to define the load excitation RMS levels, 4 samples were broken due to the fatigue damage. Then, in the final experiments, 1 fresh sample of the same batch was used. In fact, from preliminary tests and from previous research [61, 65], the vibration fatigue damage, under the loads defined in Tab. 1 and the duration discussed later in this article, can be considered negligible.
The 1st natural frequency is primarily excited in the horizontal direction and the 2nd natural frequency in the vertical direction, respectively. As the number of experiments is relatively high, special attention will be given to four experimental setups, which we denote with the level to which a particular mode is excited:

- low 1st mode - low 2nd mode: horizontal excitation 4 [N^2/Hz], vertical excitation 0.2 [$(m/s^2)^2$/Hz]
- low 1st mode - high 2nd mode: horizontal excitation 4 [N^2/Hz], vertical excitation 0.8 [$(m/s^2)^2$/Hz]
- high 1st mode - low 2nd mode: horizontal excitation 16 [N^2/Hz], vertical excitation 0.2 [$(m/s^2)^2$/Hz]
- high 1st mode - high 2nd mode: horizontal excitation 16 [N^2/Hz], vertical excitation 0.8 [$(m/s^2)^2$/Hz]

The duration of each experiment was 20 seconds. This was defined considering the required frequency resolution and the level of noise. In fact, by using the Welch method on a 20-s-long signal with 4096 points per segment, 50% overlapping (*i.e.*, 2048 points) and the Dirichlet window, the frequency resolution 400/4096=0.09765625 Hz was achieved and the noise was significantly reduced. The stress-amplitude spectrum of the four load combinations outlined above is shown in Fig. 3. The spectrum was obtained using the thermal information, combined with the thermoelastic coefficient K_m, as discussed in Sec. 2 and Sec. 3. The stress amplitude was evaluated separately at two particular locations, which correspond to the 1st and 2nd mode damage locations. In each

amplitude spectrum, two peaks (*i.e.*, at $f_1 = 33\,\text{Hz}$ and $f_2 = 55\,\text{Hz}$) due to the direct and the cross axis excitation can be observed. However, the significantly higher peak is the one that, at the particular location, corresponds to the particular mode shape. The stress-amplitude spectrum close to zero frequencies is a methodological error and corresponds to the static surface temperature.

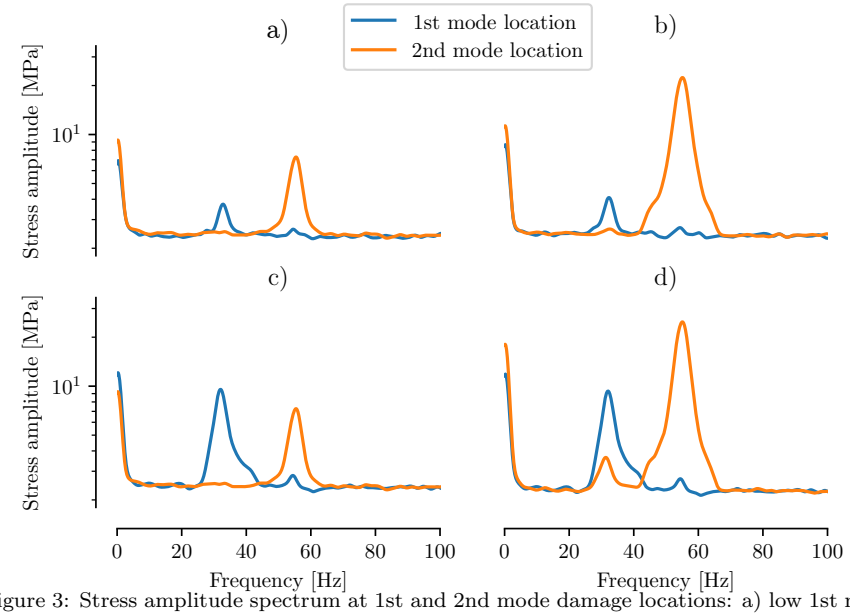

Figure 3: Stress amplitude spectrum at 1st and 2nd mode damage locations: a) low 1st mode - low 2nd mode; b) low 1st mode - high 2nd mode; c) high 1st mode - low 2nd mode; d) high 1st mode - high 2nd mode.

As discussed in Sec. 2, thermal information was used to compute the spectral moments m_i using Eq. (25). Then, the damage intensity $\bar{D}_{TB_{i,j}}$ was obtained through Tovo-Benasciutti's method using Eq. (30); this research used the fatigue parameters [66]:

$$k = 6.51 \quad B = 800.26\ [\text{MPa}] \tag{37}$$

Spatial representations of the damage intensities $\bar{D}_{TB_{i,j}}$, relative to the four experimental setups of interest presented above, are shown in Fig. 4. The damage intensity of Figs. 4 a), b) and c) was magnified to obtain more readable and comparable results.

The maximum values of the damage intensity, considering the entire thermal camera's field of view, are shown in Fig. 5 for all 16 experiments. The results at high levels of excitation directions are not consistent with our expectation; the highest damage intensity should be at the high excitation level for both natural frequencies in focus. The reason for this inconsistency can be attributed to the relatively high level of the noise in the thermal camera measurement. This noise propagates in the damage-intensity-identification method to the spectral

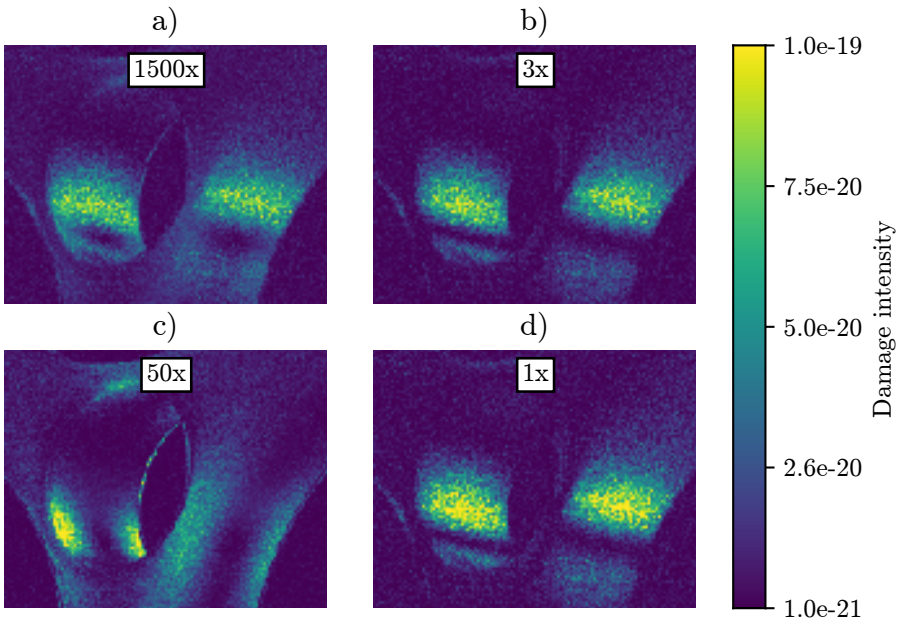

Figure 4: Estimated damage intensity in the spatial domain via Tovo-Benasciutti's method: a) low 1st mode - low 2nd mode, magnified 1500x; b) low 1st mode - high 2nd mode, magnified 3x; c) high 1st mode - low 2nd mode, magnified 50x; d) high 1st mode - high 2nd mode vertical.

moments' identification m_i (25). Outside of the natural frequencies, the spectral moments rely on relatively uncertain data, resulting in a potentially uncertain damage intensity. It is important to stress here that this uncertainty is expected to impact all the damage identification methods that rely on spectral moments (not only the one discussed here). As will be shown in the following, the modal-damage-intensity method, introduced in this research, is resistant to this uncertainty.

4.3.1. Thermoelasticity-based modal damage identification

As presented in Sec. 3, the fatigue-damage contribution $\bar{D}_{r_{i,j}}$ can be evaluated for each mode shape separately with Eq. (34). Spatial representations of the damage-intensity contribution of the 1st mode shape $\bar{D}_{1_{i,j}}$ for the selected experiments are presented in Fig. 6. For an easier comparison between the different methods and different experiments, the same scale as in Fig. 4 is used and the damage intensity is magnified. The numerical results of the $\max(\bar{D}_{1_{i,j}})$ for every combination test are presented in detail in Fig. 7.

Analogously, the fatigue-damage intensity $\bar{D}_{2_{i,j}}$ at the 2nd mode shape are presented in Figs. 8 and 9.

The modal damage intensities as presented in Figs. 6-9 are consistent with expectations. A high level of excitation always results in a higher level of damage intensity. As the excitation in the horizontal and vertical directions are slightly

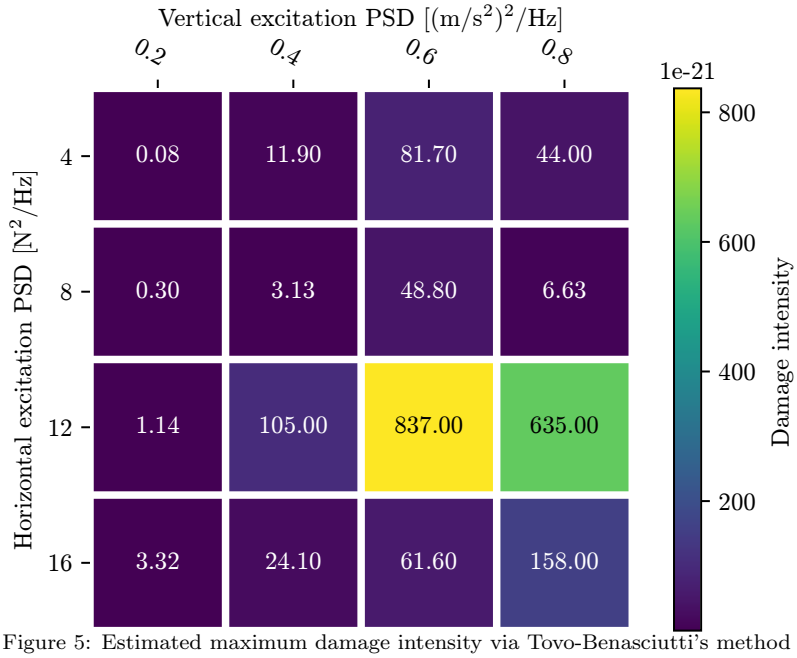

Figure 5: Estimated maximum damage intensity via Tovo-Benasciutti's method

coupled, we observe a slight increase in the damage intensity of the 2nd mode also when the excitation related to the 1st mode is increased, and vice versa. The contribution of both mode shapes $\bar{D}_{1_{i,j}} + \bar{D}_{2_{i,j}}$ is shown in Figs. 10, 11. As the modal damage identification relies on the information at resonance, the method is not impacted by the uncertainty observed in the spectral moments method.

5. Conclusions

This study researches the vibration-fatigue estimation on a flexible structure using thermal information. Time- and frequency-domain-based approaches are used to estimate the damage intensity. While the established spectral methods for the damage-intensity identification give good results with high-dynamic-range sensors (*e.g*, piezo accelerometers), these methods have a relatively large uncertainty with relatively small-dynamic-range sensors such as a thermal camera. Furthermore, the spatial information from a thermal camera can be used to obtain spatial damage-intensity information. Based on the recently presented modal-damage-decomposition approach, this research introduces a modal-damage-intensity identification based on the thermoelastic principle. Due to the fact that the modal-damage-intensity method relies on the modal information at the natural frequency, the uncertainty is reduced, if compared to classic spectral methods. More importantly, the damage intensity can be decomposed to particular mode shapes. With the modal damage information, the source of the

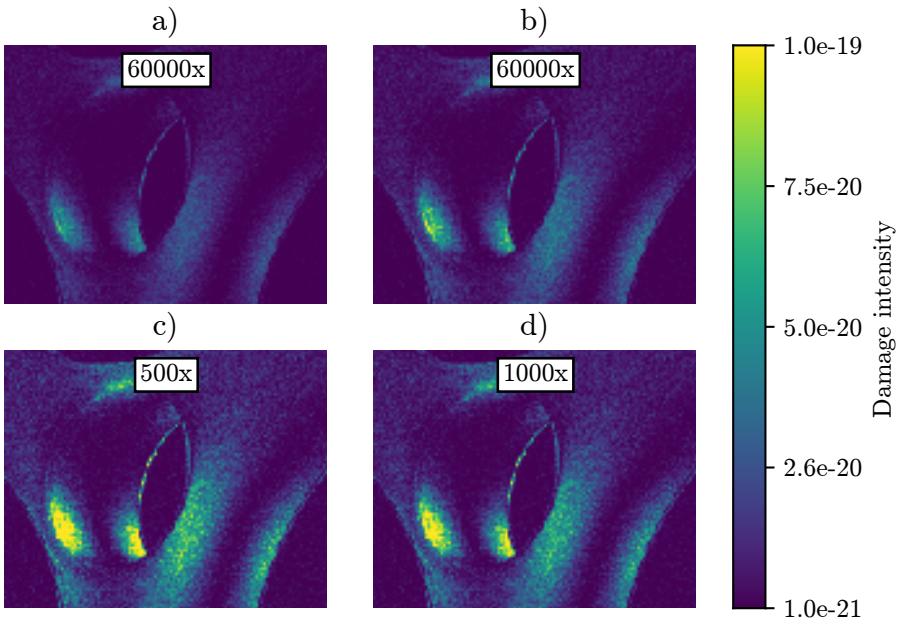

Figure 6: Estimated modal damage intensity $\bar{D}_{1_{i,j}}$ in the spatial domain caused by the 1st mode shape: a) low 1st mode - low 2nd mode, magnified 60000x; b) low 1st mode - high 2nd mode, magnified 60000x; c) high 1st mode - low 2nd mode, magnified 500x; d) high 1st mode - high 2nd mode, magnified 1000x.

damage is clearly revealed.
Experimental research using an aluminum alloy Y-shaped specimen under multiaxial excitation is presented. A total of 16 different excitation setups, resulting in different levels of modal damage, were researched. The modal-damage-identification method was compared with the established spectral methods.

Acknowledgement

The authors acknowledge the partial financial support of the Slovenian Research Agency (research core funding no. P2-0263 and project J2-1730).

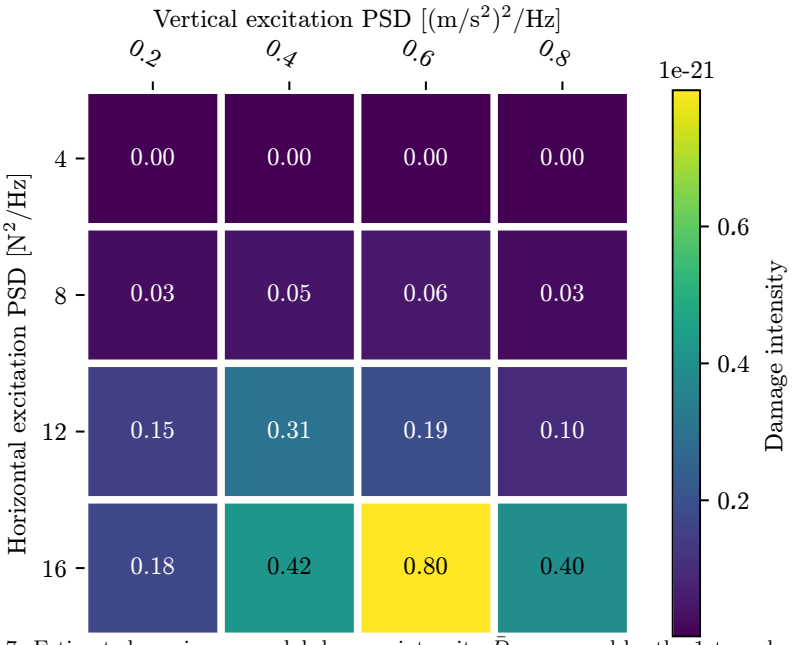

Figure 7: Estimated maximum modal damage intensity $\bar{D}_{1_{i,j}}$ caused by the 1st mode shape

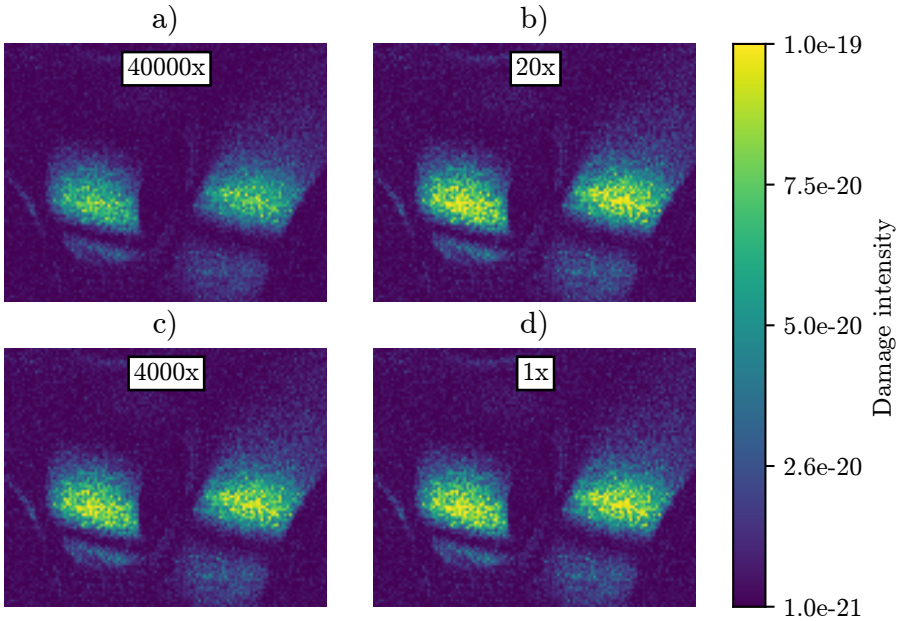

Figure 8: Estimated damage intensity $\bar{D}_{2_{i,j}}$ in spatial domain caused by the 2nd mode shape: a) low 1st mode - low 2nd mode, magnified 40000x; b) low 1st mode - high 2nd mode, magnified 20x; c) high 1st mode - low 2nd mode, magnified 4000x; d) high 1st mode - high 2nd mode.

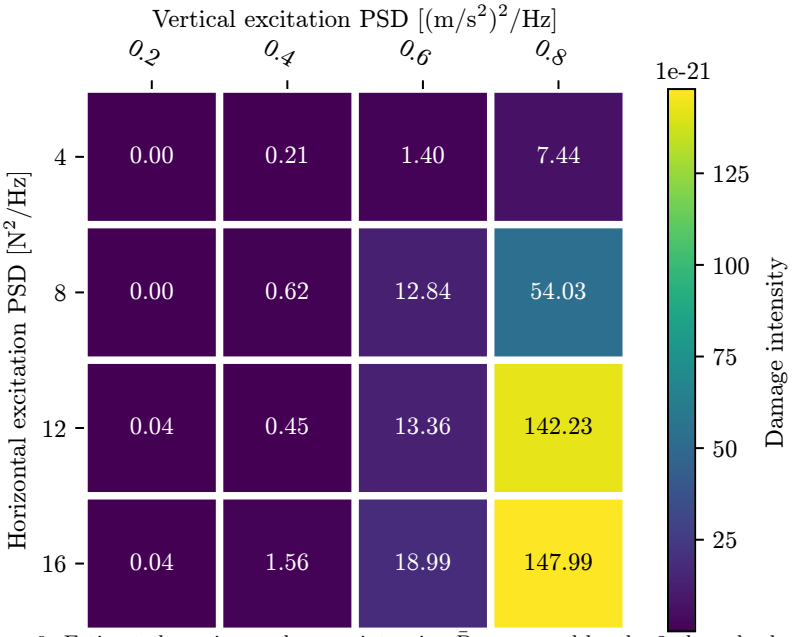

Figure 9: Estimated maximum damage intensity $\bar{D}_{2_{i,j}}$ caused by the 2nd mode shape

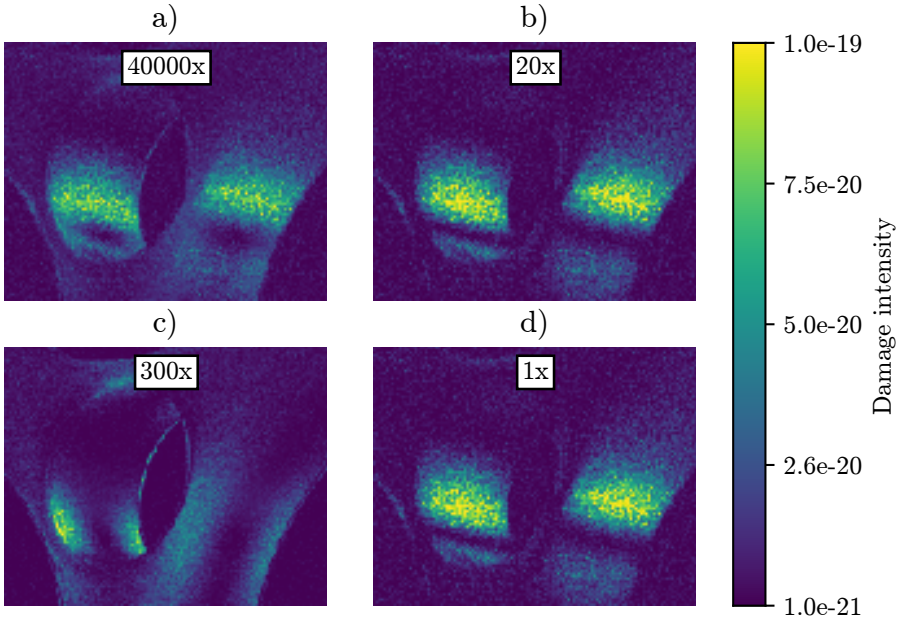

Figure 10: Estimated total damage intensity $\bar{D}_{1_{i,j}} + \bar{D}_{2_{i,j}}$ in the spatial domain via the modal identification approach: a) low 1st mode - low 2nd mode, magnified 50000x; b) low 1st mode - high 2nd mode, magnified 20x; c) high 1st mode - low 2nd mode, magnified 300x; d) high 1st mode - high 2nd mode.

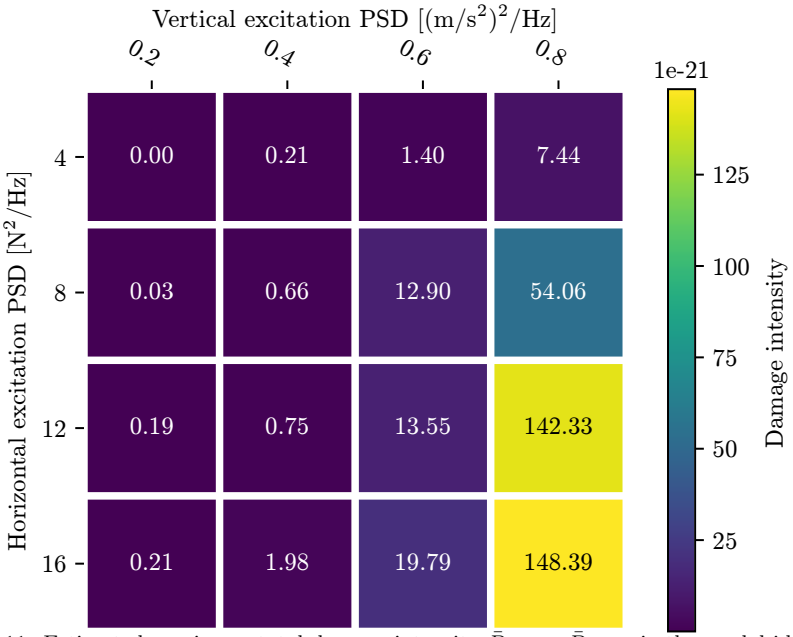

Figure 11: Estimated maximum total damage intensity $\bar{D}_{1_{i,j}} + \bar{D}_{2_{i,j}}$ via the modal identification approach

References

[1] D. Benasciutti, F. Sherratt, and A. Cristofori. Basic Principles of Spectral Multi-axial Fatigue Analysis. *Procedia Engineering*, 101:34–42, 2015.

[2] P. Wolfsteiner and A. Trapp. Fatigue life due to non-Gaussian excitation–An analysis of the Fatigue Damage Spectrum using Higher Order Spectra. *International Journal of Fatigue*, 127:203–216, 2019.

[3] M. Mršnik, J. Slavič, and M. Boltežar. Frequency-domain methods for a vibration-fatigue-life estimation–Application to real data. *International Journal of Fatigue*, 47:8–17, 2013.

[4] D. Benasciutti and R. Tovo. Spectral methods for lifetime prediction under wide-band stationary random processes. *International Journal of Fatigue*, 27(8):867–877, 2005.

[5] J. Slavič, M. Mršnik, M. Česnik, J. Javh, and M. Boltežar. *Vibration Fatigue by Spectral Methods: From Structural Dynamics to Fatigue Damage*. Elsevier (In Press), 2020.

[6] G. Petrucci and B. Zuccarello. Fatigue life prediction under wide band random loading. *Fatigue & Fracture of Engineering Materials & Structures*, 27(12):1183–1195, 2004.

[7] R. C. Ugras, O. K. Alkan, S. Orhan, M. Kutlu, and A. Mugan. Real time high cycle fatigue estimation algorithm and load history monitoring for vehicles by the use of frequency domain methods. *Mechanical Systems and Signal Processing*, 118:290–304, 2019.

[8] R. Tovo. Cycle distribution and fatigue damage under broad-band random loading. *International Journal of Fatigue*, 24(11):1137–1147, 2002.

[9] T. Dirlik. *Application of computers in fatigue analysis*. PhD thesis, University of Warwick, 1985.

[10] Z. Gao and T. Moan. Frequency-domain fatigue analysis of wide-band stationary Gaussian processes using a trimodal spectral formulation. *International Journal of Fatigue*, 30(10-11):1944–1955, 2008.

[11] P.H. Wirsching and M. C. Light. Fatigue under wide band random stresses. *Journal of the Structural Division*, 106(7):1593–1607, 1980.

[12] W. Zhao and M. J. Baker. On the probability density function of rainflow stress range for stationary Gaussian processes. *International Journal of Fatigue*, 14(2):121–135, 1992.

[13] C. Braccesi, G. Morettini, F. Cianetti, and M. Palmieri. Evaluation of fatigue damage with an energy criterion of simple implementation. *Procedia Structural Integrity*, 8:192–203, 2018.

[14] D. Gao, W. Yao, and T. Wu. A damage model based on the critical plane to estimate fatigue life under multi-axial random loading. *International Journal of Fatigue*, 129:104729, 2019.

[15] D. Benasciutti, D. Zanellati, and A. Cristofori. The "Projection-by-Projection" (PbP) criterion for multiaxial random fatigue loadings. *Frattura ed Integrità Strutturale*, 13(47):348–366, 2019.

[16] Y. Zhou and J. Tao. Theoretical and numerical investigation of stress mode shapes in multi-axial random fatigue. *Mechanical Systems and Signal Processing*, 127:499–512, 2019.

[17] D. Benasciutti, J. Srnec Novak, L. Moro, F. De Bona, and A. Stanojević. Experimental characterisation of a CuAg alloy for thermo-mechanical applications. Part 1: Identifying parameters of non-linear plasticity models. *Fatigue & Fracture of Engineering Materials & Structures*, 41(6):1364–1377, 2018.

[18] M. Mršnik, J. Slavič, and M. Boltežar. Multiaxial vibration fatigue—A theoretical and experimental comparison. *Mechanical Systems and Signal Processing*, 76:409–423, 2016.

[19] G. Morettini, C. Braccesi, F. Cianetti, S.M. Javad Razavi, K. Solberg, and L. Capponi. Collection of experimental data for multiaxial fatigue criteria verification. *Fatigue & Fracture of Engineering Materials & Structures*, 43(1):162–174, 2020.

[20] M. Mršnik, J. Slavič, and M. Boltežar. Vibration fatigue using modal decomposition. *Mechanical Systems and Signal Processing*, 98:548–556, 2018.

[21] T. C. Chu, W. F. Ranson, and A. Sutton. Applications of digital-image-correlation techniques to experimental mechanics. *Experimental mechanics*, 25(3):232–244, 1985.

[22] B. D. Lucas and T. Kanade. An iterative image registration technique with an application to stereo vision. *Proceedings DARPA Image Understanding Workshop*, pages 121–130, 1981.

[23] J. Javh, J. Slavič, and M. Boltežar. High frequency modal identification on noisy high-speed camera data. *Mechanical Systems and Signal Processing*, 98:344–351, 2018.

[24] D. Gorjup, J. Slavič, and M. Boltežar. Frequency domain triangulation for full-field 3D operating-deflection-shape identification. *Mechanical Systems and Signal Processing*, 133:106287, 2019.

[25] J. Baqersad, P. Poozesh, C. Niezrecki, and P. Avitabile. Photogrammetry and optical methods in structural dynamics–A review. *Mechanical Systems and Signal Processing*, 86:17–34, 2017.

[26] S. Gholizadeh. A review of non-destructive testing methods of composite materials. *Procedia Structural Integrity*, 1:50–57, 2016.

[27] W. Weber. Über die specifische Wärme fester Körper, insbesondere der Metalle. *Annalen der Physik*, 96(10):177–213, 1830.

[28] W. Thomson. On the Dynamical Theory of Heat. *Earth and Environmental Science Transactions of The Royal Society of Edinburgh*, 20(2):261–288, 1853.

[29] X. Guo and Y. Mao. Defect identification based on parameter estimation of histogram in ultrasonic IR thermography. *Mechanical Systems and Signal Processing*, 58:218–227, 2015.

[30] G. Allevi, L. Capponi, P. Castellini, P. Chiariotti, F. Docchio, F. Freni, R. Marsili, M. Martarelli, R. Montanini, and S. Pasinetti. Investigating additive manufactured lattice structures: a multi-instrument approach. *IEEE Transactions on Instrumentation and Measurement*, 2019.

[31] X. D. Li, H. Zhang, D. L. Wu, X. Liu, and J. Y. Liu. Adopting lock-in infrared thermography technique for rapid determination of fatigue limit of aluminum alloy riveted component and affection to determined result caused by initial stress. *International Journal of Fatigue*, 36(1):18–23, 2012.

[32] J. Qiu, C. Pei, H. Liu, and Z. Chen. Quantitative evaluation of surface crack depth with laser spot thermography. *International Journal of Fatigue*, 101:80–85, 2017.

[33] Y. Li, R. Zhang, L. Li, P. Bao, W. Zhang, Z. Yang, G. Tian, and A. Ming. Temperature variation and damage characteristic of impacted CFRP laminate using infrared thermography: Experimental investigation. *International Journal of Fatigue*, 112:130–137, 2018.

[34] G. Fargione, A. Geraci, G. La Rosa, and A. Risitano. Rapid determination of the fatigue curve by the thermographic method. *International Journal of Fatigue*, 24(1):11–19, 2002.

[35] W. Yang, X. Guo, Q. Guo, and J. Fan. Rapid evaluation for high-cycle fatigue reliability of metallic materials through quantitative thermography methodology. *International Journal of Fatigue*, 124:461–472, 2019.

[36] Z. Stankovičová, V. Dekýš, P. Novák, and B. Strnadel. Detection of Natural Frequencies Using IR Camera. *Procedia Engineering*, 192:830–833, 2017.

[37] C. Braccesi, F. Cianetti, G. Lori, and D. Pioli. Random multiaxial fatigue: A comparative analysis among selected frequency and time domain fatigue evaluation methods. *International Journal of Fatigue*, 74:107–118, 2015.

[38] K. T. Compton and D. B. Webster. Temperature changes accompanying the adiabatic compression of steel. *Physical Review*, 5(2):159, 1915.

[39] R. T. Potter and L. J. Greaves. The application of thermoelastic stress analysis techniques to fibre composites. In *Optomechanical systems engineering*, volume 817, pages 134–146. International Society for Optics and Photonics, 1987.

[40] A. K. Wong, J. G. Sparrow, and S. A. Dunn. On the revised theory of the thermoelastic effect. *Journal of Physics and chemistry of solids*, 49(4):395–400, 1988.

[41] W. N. Sharpe. *Springer handbook of experimental solid mechanics*. Springer Science & Business Media, 2008.

[42] J. M. Dulieu-Barton and P. Stanley. Development and applications of thermoelastic stress analysis. *The Journal of Strain Analysis for Engineering Design*, 33(2):93–104, 1998.

[43] G. M. Carlomagno and P. G. Berardi. Unsteady thermotopography in non-destructive testing. In *Proc. 3rd Biannual Exchange, St. Louis/USA*, volume 24, page 26, 1976.

[44] N. Harwood and W. M. Cummings. Applications of thermoelastic stress analysis. *Strain*, 22(1):7–12, 1986.

[45] N. Harwood and W. M. Cummings. Calibration of the thermoelastic stress analysis technique under sinusoidal and random loading conditions. *Strain*, 25(3):101–108, 1989.

[46] K. Shin and J. Hammond. *Fundamentals of signal processing for sound and vibration engineers*. John Wiley & Sons, 2008.

[47] G. M. Jenkins and D. G. Watts. Spectral Analysis and its Applications Holden-Day, San Francisco. *Spectral analysis and its application. Holden-Day, San Francisco.*, 1968.

[48] P. Welch. The use of fast Fourier transform for the estimation of power spectra: a method based on time averaging over short, modified periodograms. *IEEE Transactions on audio and electroacoustics*, 15(2):70–73, 1967.

[49] P. Virtanen, R. Gommers, T. Oliphant, M. Haberland, T. Reddy, D. Cournapeau, E. Burovski, P. Peterson, W. Weckesser, J. Bright, S. van der Walt, M. Brett, J. Wilson, K. J. Millman, N. Mayorov, A.R. J. Nelson, E. Jones, R. Kern, E. Larson, C. J. Carey, İ. Polat, Y. Feng, E. Moore, J. VanderPlas, D. Laxalde, J. Perktold, R. Cimrman, I. Henriksen, E. A. Quintero, C. Harris, A. Archibald, A. Ribeiro, F. Pedregosa, P. van Mulbregt, A. Vijaykumar, A. P. Bardelli, Al. Rothberg, A. Hilboll, A. Kloeckner, A. Scopatz, A. Lee, A. Rokem, C. Woods, C. Fulton, C. Masson, C. Häggström, C. Fitzgerald, D. Nicholson, D. Hagen, D. Pasechnik, E. Olivetti, E. Martin, E. Wieser, F. Silva, F. Lenders, F. Wilhelm, G. Young, G. Price, G. L. Ingold, G. E. Allen, G. R. Lee, H. Audren, I. Probst, J. P. Dietrich,

J. Silterra, J. T. Webber, J. Slavič, J. Nothman, J. Buchner, J. Kulick, J. L. Schönberger, J. V. de Miranda Cardoso, J. Reimer, J. Harrington, J. L. C. Rodríguez, J. Nunez-Iglesias, J. Kuczynski, K. Tritz, M. Thoma, M. Newville, M. Kümmerer, M. Bolingbroke, M. Tartre, M. Pak, N.J. Smith, N. Nowaczyk, N. Shebanov, O. Pavlyk, P. A. Brodtkorb, P. Lee, R. T. McGibbon, R. Feldbauer, S. Lewis, S. Tygier, S. Sievert, S. Vigna, S. Peterson, S. More, T. Pudlik, T. Oshima, T. Pingel, T. Robitaille, T. Spura, T. Jones, T. Cera, T. Leslie, T. Zito, T. Krauss, U. Upadhyay, Y. O. Halchenko, and Y. Vázquez-Baeza. SciPy 1.0: fundamental algorithms for scientific computing in Python. *Nature Methods*, 2020.

[50] N. M. M. Maia and J. M. M. Silva. *Theoretical and experimental modal analysis*. Research Studies Press, 1997.

[51] O. Bernasconi and D. J. Ewins. Modal strain/stress fields. *International Journal of Analytical and Experimental Modal Analysis*, 4:68–76, 1989.

[52] A. Preumont and V. Piefort. Predicting random high-cycle fatigue life with finite elements. *Journal of Vibration and Acoustics, Transactions of the ASME*, 116:2, 1994.

[53] T. Kranjc, J. Slavič, and M. Boltežar. A comparison of strain and classic experimental modal analysis. *Journal of Vibration and Control*, 22(2):371–381, 2016.

[54] R. J. Guyan. Reduction of stiffness and mass matrices. *AIAA journal*, 3(2):380, 1965.

[55] R. C. Juvinall and K. M. Marshek. *Fundamentals of machine component design*, volume 83. John Wiley & Sons New York, 2006.

[56] O. H. Basquin. The exponential law of endurance tests. In *ASTM*, volume 10, page 625, 1910.

[57] J. S. Bendat and A. G. Piersol. *Random data analysis and measurement procedures*. Wiley & Sons, New York, fourth edition, 2000.

[58] J. M. Dulieu-Smith. Alternative calibration techniques for quantitative thermoelastic stress analysis. *Strain*, 31(1):9–16, 1995.

[59] R. D. Mindlin and N. N. Eshel. On first strain-gradient theories in linear elasticity. *International Journal of Solids and Structures*, 4(1):109–124, 1968.

[60] D. Benasciutti and R. Tovo. Frequency-based fatigue analysis of non-stationary switching random loads. *Fatigue & Fracture of Engineering Materials & Structures*, 30(11):1016–1029, 2007.

[61] L. Capponi, M. Česnik, J. Slavič, F. Cianetti, and M. Boltežar. Non-stationarity index in vibration fatigue: Theoretical and experimental research. *International Journal of Fatigue*, 104:221–230, 2017.

[62] A. K. Mackenzie. Effects of surface coatings on infra-red measurements of thermoelastic responses. In *Stress and Vibration: Recent Developments in Industrial Measurement and Analysis*, volume 1084, pages 59–71. International Society for Optics and Photonics, 1989.

[63] J. McKelvie. Consideration of the surface temperature response to cyclic thermoelastic heat generation. In *Society of Photo-Optical Instrumentation Engineers (SPIE) Conference Series*, volume 731, pages 44–55, 1987.

[64] R. Marsili, G. Rossi, and E. Speranzini. Study of the causes of uncertainty in thermoelasticity measurements of mechanical components. *Measurement*, 118:230–236, 2018.

[65] M. Česnik, J. Slavič, L. Capponi, M. Palmieri, F. Cianetti, and M. Boltežar. The relevance of non-stationarities and non-Gaussianities in vibration fatigue. In *MATEC Web of Conferences*, volume 165, 2018.

[66] P. Ogrinec, J. Slavič, M. Česnik, and M. Boltežar. Vibration fatigue at half-sine impulse excitation in the time and frequency domains. *International Journal of Fatigue*, 123:308–317, 2019.